Version of Record: https://www.sciencedirect.com/science/article/pii/S0038092X20310355
Manuscript_b5832612b62a4c7925abfef1363ffa04

Annual Simulation of Photovoltaic Retrofits within Existing Parabolic Trough Concentrating Solar Powerplants

Nipun Goel[1*], Hannah O'Hern[2], Matthew Orosz[2], Todd Otanicar[1]

[1]Department of Mechanical and Biomedical Engineering, Boise State University

[2]Department of Mechanical Engineering, The University of Tulsa

*corresponding author: nipungoel@boisestate.edu

Abstract

Solar power for electricity production comes from either photovoltaics or concentrating solar power plants. The former has seen rapid growth and expansion due to the rapid fall in global prices, while the latter has seen moderate growth due to ability to cheaply store thermal energy for later use. Hybridization, or combining photovoltaics with concentrating solar power represents a potential way for lowering cost while enabling long term storage. Over 5 GW of capacity exist worldwide using parabolic trough style technology for concentrating solar power which presents a unique option for optimization in the form of a photovoltaic retrofit. While it is possible to analyze the performance with detailed physics models, it is necessary to create a model that can handle simulating the plant level performance to fully understand the potential performance. Here, the first utility scale plant level model of a hybrid photovoltaic-concentrating solar power plant is developed. The model is applied to existing concentrating solar power plants around the world utilizing RP-3 mirrors without thermal energy storage to understand the impact on electricity production. Model results indicate that the photovoltaic retrofit can increase yearly electricity

© 2020 published by Elsevier. This manuscript is made available under the Elsevier user license
https://www.elsevier.com/open-access/userlicense/1.0/

production by up to 30% for plants with solar multiples exceeding 1.5, and that increasing the fraction of solar energy reflected further increases the yield. The increased electrical production declines as the plant solar multiple is decreased. The minimum LCOE observed was $0.07/kWh for plants with larger solar multiple and fraction of solar energy reflected to the PV is 50% of the total aperture.

Keywords: concentrating solar power; photovoltaics; retrofit; simulation

Nomenclature:

Symbols

$A_{aperture}$	Field Aperture Area
B	Daily Angle
C_{CPV}	Capital Cost for PV retrofit
$C_{inverter}$	Inverter Cost
$C_{O\&M}$	Operation and Maintenance Cost
C_{soft}	Soft Costs
w_{PV}	Width of PV
$C_{dichroic}$	Cost of Dichroic
$C_{extrusion}$	Cost of Extrusion
C_{cell}	Cost of PV Cell
CSP_e	Total Electrical power generated from CSP
CSP_{out}	Net Electrical power output from CSP power block
CSP_{net}	Overall Net Electrical power output from CSP plant
$L_{dichroic}$	Length of Dichroic

i	Rate of interest
N	number of years
DNI_{norm}	Solar Flux delivered to the CSP HCE
DNI_{CSP}	Solar Flux transmitted to CSP through the Dichroic mirrors
EoT	Equation of Time
EQE_{λ}	Spectral External Quantum Efficiency
f_{dust}	Mirror Soiling
f_{conc}	Concentration Factor
f_{avail}	Solar Field Availability
$f_{bellows}$	Bellows Shadowing
$f_{dichroic}$	flux line fraction intercepted by the dichroic mirror
$F_{constant_loss}$	CSP system Constant Losses Factor
F_{HL_A0} .. F_{HL_A6}	A0 Heat Loss Coefficient through A6 Heat Loss Coefficient
FF	Fill Factor
FF_{ref}	Fill Factor at the reference condition
I_{sc}	Short-Circuit Current
$LCOE$	Levelized Cost of Electricity
L_{SCA}	Length of SCA
$P_{inc,CSP}$	Solar Power Incident on HCE
P_{loss}	Parasitic Loss
$P_{loss,system\ design}$	System Design Parasitic Losses
PV_{out}	Net Power output from PV

$\dot{Q_{design}}$	Turbine Design Cycle Thermal Energy Input
Q_{HCEHL}	Average Integrated HCE Heat Loss
Q_{HCE_loss}	Total HCE Heat Loss
Q_{Net}	Net Solar Field Thermal Power Output
$\dot{Q_{pb}}$	Thermal Energy to Power Block
Q_{pipe_loss}	Piping Heat Loss
$Q_{PHL_DesignT}$	Piping Heat Loss Coefficient at Design Temperature
$Q_{SF,design}$	Design Solar Field Thermal Energy
$Q_{thermal}$	Total Solar Field Thermal Power Output
SCA_{factor}	MWe power required per unit field aperture area
T_{SF_in}	Solar Field HCE Receiver Inlet Temperature
T_{SF_out}	Solar Field HCE Receiver Outlet Temperature
T_{amb}	Ambient Temperature
T_{PV}	PV Module Temperature
T_{ref}	Reference Temperature
t_{sol}	Solar Time
V_{OC}	Open Circuit Voltage
$V_{oc,ref}$	Reference Open Circuit Voltage
v_w	Wind speed
$\dot{W}_{gr,design}$	Design Gross Cycle Output
$\overline{\dot{W_{gr}}}$	Non-Dimensional Gross Cycle Output
$\dot{W}_{net}$	Net Cycle Power Output

$x_{coverage}$	Fraction SCA length covered by PV cells

Greek Symbols

ϕ	Latitude
ϕ_λ	Spectral Photon Flux
ψ	Longitude
ψ_{TZM}	longitude of time-zone meridian
ω	Hour Angle
δ	Declination Angle
θ_z	Zenith Angle
θ_e	Solar Elevation
γ_{sol}	Solar Azimuthal Angle
ω_{col}	Collector Tracking Angle
θ	Angle of Incidence
γ_{col}	Collector Azimuthal Angle
θ_{col}	Collector Tilt Angle
η_{track}	Tracking Error
η_{geo}	Geometry Defects
ρ_M	Mirror Reflectance
ρ_{sw}	Solar Weighted Reflectance
η_{carnot}	Carnot Efficiency
$\eta_{IAM}(\theta)$	Incidence Angle Modifier

η_{opt}	Overall Optical Efficiency
η_{opt_HCE}	Optical Efficiency of Heat Collecting Elements
$\eta_{opt,dichroic}$	Optical Efficiency of Dichroic Mirrors
τ_e	Envelope Transmittivity
α_a	Absorber Absorption
β_{VOC}	Open Circuit Voltage Temperature Coefficient
β_{FF}	Fill Factor Temperature Coefficient
$\beta_{P,max}$	Temperature Coefficient at Maximum Power Point
β_{JSC}	Temperature Coefficient of Short-Circuit Current Density
$X_{DC-wiring}$	DC wiring losses of PV module
X_{MPPT}	MPPT Effectiveness Losses
X_{module}	Module Mismatch Derating

Abbreviations

BoP	Balance of Plant
CPV/T	Concentrating Photovoltaic/Thermal
CSP	Concentrated Solar Power
CT	Cooling Tower
DNI	Direct Normal Solar Irradiance
HCE	Heat Collecting Element
HTF	Heat Transfer Fluid
LCOE	Levelized Cost of Energy

NB	No Benefit
PB	Power Block
PV	Photovoltaic
PVR	Photovoltaic Receiver
SAM	System Advisor Model
SCA	Solar Collector Assembly
TES	Thermal Energy Storage
TMY	Typical Meteorological Year

1. Introduction

Photovoltaic (PV) power plants continue to grow worldwide due to maturation of the technology, and declining costs, but PV power input into the grid is dictated by the availability of sunlight and largely weakens the dispatchability of the grid. Global PV installation saw an increase of approximately 392 GW from 2006 to 2017, with projected growth up to 575 GW of additional infrastructure by 2023 (Birol, 2018). This has motivated grid scale energy storage research for solar energy production to decouple the load and dispatchability of the operator. While grid scale batteries have been recently introduced into the market (Penn, 2017), concentrated solar power (CSP), which converts sunlight to thermal energy before final conversion to electrical energy, has a mature energy storage technology in thermal energy storage (TES) which has been routinely deployed at over 100MW and 1000MWh at Solana, Crescent Dunes, Andasol, Extresol and other sites (Variés, 2009). CSP technology has extensive infrastructure with 5.5 GW of operational capacity installed worldwide to generate reliable power (SolarPACES, 2019). Of the total installed capacity, 3.6 GW or 66% result from parabolic trough plants that utilize inner and outer sets of

RP3 mirrors. The main drawback of CSP is that the installed cost is on the order of two to three times higher than for PV power plants of similar capacity (Orosz, 2015).

Because of these differences in cost, hybridization of CSP and PV is of growing interest for lowering the levelized cost of electricity (LCOE) and for potentially enhancing power plant output. Hybrid CSP-PV has seen a number of recent efforts for both pure power generation and for potential in the process heat industry. Hybrid receivers are capable of utilizing all the wavelengths of the solar spectrum while providing electricity that is dispatchable (Branz et al., 2015). A number of different approaches for the hybridization of CSP and PV exist. One common approach is to use spectral splitting with dichroic mirrors to focus a portion of the sunlight on a PV receiver while transmitting the rest to a CSP receiver (Fisher and Biddle, 2011; Orosz et al., 2016a; Widyolar et al., 2018). Another approach is to use the inherent spectrally selective nature of PV cells to partially transmit concentrated sunlight through a PV receiver to a thermal receiver (Robertson et al., 2019; Xu et al., 2016). A third approach is to utilize the heat transfer fluid of the receiver to act as spectrally selective element directly (An et al., 2017; Crisostomo et al., 2017; Goel et al., 2020; Todd Otanicar et al., 2018). The majority of the previously cited work here has focused on detailed analysis and experimental testing of these hybrid CSP-PV concepts, with limited investigation of the full powerplant level effects of a hybrid CSP-PV system in a comprehensive side by side comparison. This is particularly relevant for one of the approaches that is designed to act as a retrofit for existing CSP powerplants (O'Hern et al., 2018; T Otanicar et al., 2018). The retrofit approach is particularly relevant as a number of CSP plants using parabolic trough are approaching design lifetimes and/or the completion of their Power Purchase Agreement (PPA) effective period, motivating operators to consider strategic options including decommissioning, upgrading or repowering, and revised commercial arrangements such as feed in tariffs (O'Hern et al., 2018).

Recently, one of the Solar Energy Generating Stations (SEGS) plants was taken offline, torn down, and replaced with a PV powerplant (O'Hern et al., 2018). This motivates further study about the potential for a retrofit, where understanding of power production at a plant level is needed.

Existing work in simulating hybrid CSP-CPV systems investigate dispatch strategy of the storage for physically separated CSP and CPV systems such as shown in a recent comparison (using Matlab) for the Ottana Solar Facility (Cocco et al., 2016) and for Ouarzazate Morocco (Petrollese and Cocco, 2016). Another study utilized TRNSYS to optimize the sizing of the PV field for both LCOE and capacity factor when integrated as physically separate installations in northern Chile (Starke et al., 2018). Another study utilized TRNSYS to simulate a trigeneration solar collector based upon linear Fresnel concentrators focused on a PV receiver with active heat removal (Moaleman et al., 2018). The resulting systems investigate the cooling, heating, and electrical energy (via the PV) but do not consider spectral splitting or generation of electricity from the thermal energy (Moaleman et al., 2018). A true hybrid concentrating photovoltaic/thermal (CPV/T) system was recently investigated for a combined heat and power in dairy farms(Wang et al., 2019). The system employed a spectrum splitting approach to reflect light to the PV cell while capturing thermal energy in the absorber for creation of steam for dairy farm use. The simulation was conducted over a full year to provide detailed thermal and electrical outputs (Wang et al., 2019). Notably, no production of electrical energy from the high temperature thermal energy was considered.

In addition to the works noted above, there are many commercial software packages available to determine the hourly output of commercial plants using solar energy (both PV and CSP separately). The System Advisor Model (SAM) is a free software developed by NREL (National Renewable Energy Laboratory, 2016) that is utilized for both performance and detailed financial

modeling. While SAM and other specialized tools are capable of modeling PV, parabolic trough CSP, tower CSP, and CPV plants, there is no commercially available platform that can simulate a hybrid of both CSP and CPV when the two systems are physically coupled. Because there are no commercial packages that can fully handle a hybrid CSP-CPV analysis, custom models are developed that utilize first-principles in physics and heat transfer to predict the performance of such systems. These approaches result in computationally demanding models that are almost exclusively used for steady state single operational point performance simulation. Because of the computational intensity of these physics-based models, yearlong yield analyses become problematic for rapid assessment of system design, and deployment. Additionally, they rarely consider the additional losses associated with a full-scale power plant, such as inverter losses, wiring losses, and reduction in power block effectiveness from reduced heat load. Further, to our knowledge no prior work has studied the hourly performance potential of a hybrid CSP-PV system using dichroic mirrors for applications in pure electricity generation.

In this work we develop a framework to assess the yearly yield of the hybrid CSP-PV system based on the retrofit design (Orosz et al., 2016a). The model approach builds off the existing approach used for modeling the performance of a CSP powerplant in the SAM tool (Michael J. and Gilman, 2011) and couples to this a semi-detailed model for the performance of a PV module under concentrated spectrally split sunlight. The CSP portion of the model is validated against existing CSP models and actual plant data. The model is then applied to a number of specific plants that utilize RP-3 mirror geometry, as this is the mirror geometry for which the proposed retrofit is designed (O'Hern et al., 2017). To our knowledge this is the first model built for this level of plant analysis for a hybrid CSP-PV system. The model is used to assess the role of the originally designed plant solar multiple, and dichroic mirror coverage of the reflected incidence to model the

impact on overall yearly electricity production from the combined PV+CSP plant. Figure 1 provides a schematic of the CSP-PV hybrid explored in this work and (b) shows the PV retrofit system as built and tested.

a)

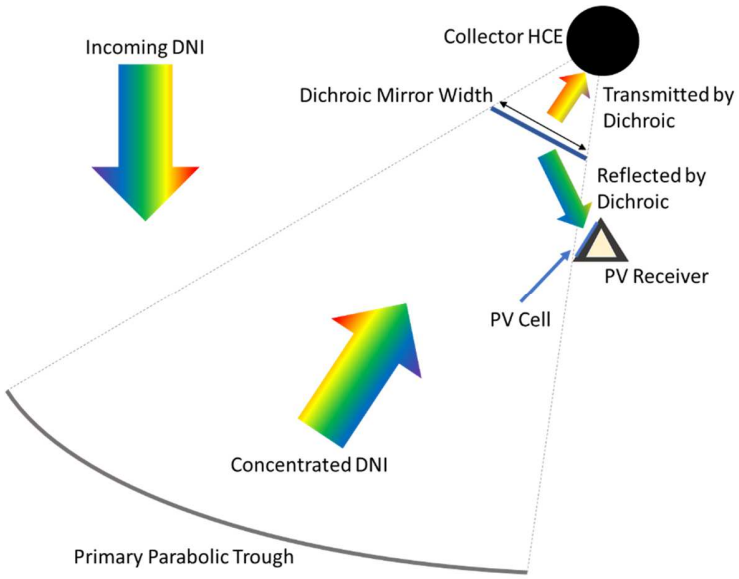

b)

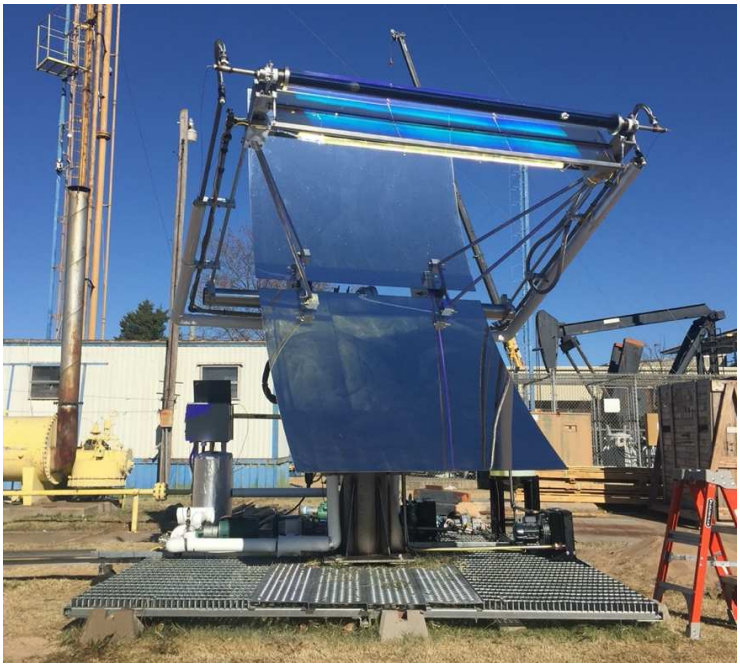

Figure 1: a) Schematic of CSP-PV hybrid retrofit concept for parabolic trough style powerplants. (Note only half the primary mirror aperture is shown, and for this configuration the dichroic intercepts all of the incoming concentrated DNI ($f_{dichroic}$=1)) and b) as built and tested PV retrofit for CSP.

2. CSP Plant Model

The CSP plant model is developed from the existing empirical model used within SAM for which detailed equations can be found in the SAM technical manual (Michael J. and Gilman, 2011). The two key pieces in a concentrated solar power plant are the solar field (comprised of the primary optics, heat collection element, and through which the heat transfer fluid flows), and the power block (which converts the solar generated thermal energy into electrical energy). A detailed framework for simulation of a CSP plant is provided in Figure 2 with subsequent relevant equations in different components in the solar field and the power block covered in detail in the subsequent sections. These equations impact the overall plant performance and are also impacted by the addition of the PV hybridization, as shown later.

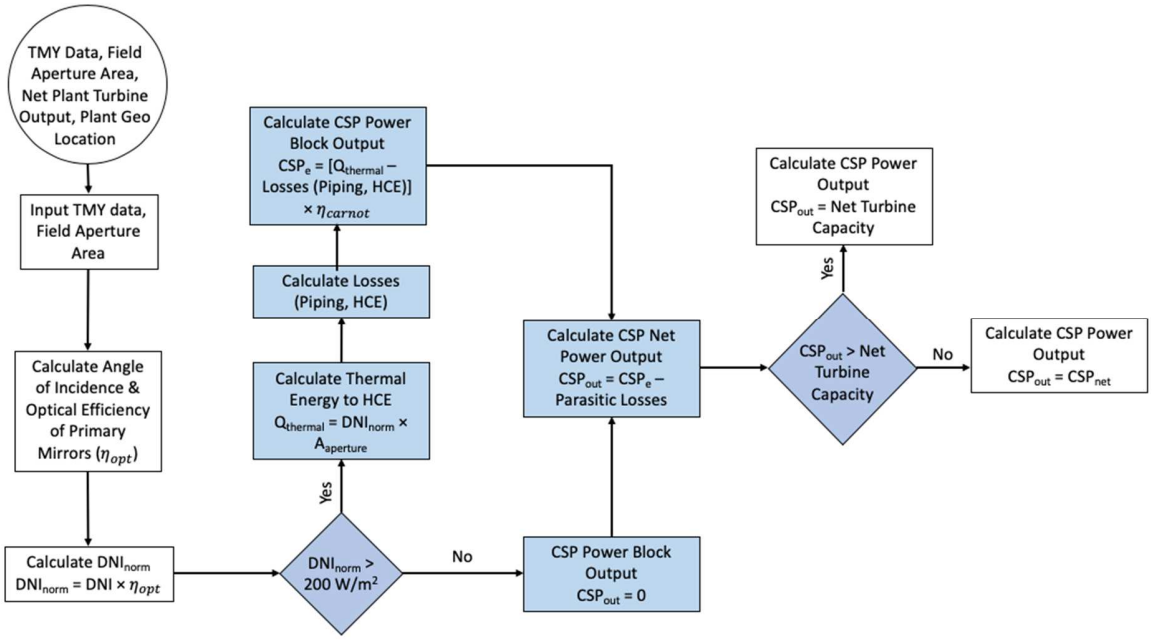

Figure 2: Framework of hourly simulation of CSP collector for existing parabolic trough style powerplants.

The algorithm uses geographical information, meteorological data, and the solar field specifications to calculate the corresponding solar time and angle of incidence of the solar radiation

on a collector operating on sun-tracking mode (detailed calculations are provided in Supplemental Material). The solar flux thus obtained is used with the field optical efficiency (Section 2.2), and the field thermal losses (Section 2.3) to obtain the useful thermal power delivered by the solar field. These results are then used to calculate the gross electric power generated (Section 2.4), the plant's parasitic losses (Section 2.5) and, finally, the net electricity production.

2.1. Geographical Location and Meteorological data

The geographical location of the plant is used to calculate the solar time, which is the time based on the angular motion of the sun with respect to the location of the site. The geographical location is the latitude (ϕ), and longitude (ψ) at the site, and the longitude of the corresponding time-zone meridian (ψ_{TZM}).

Typical Meteorological Year (TMY) data for the chosen locations was downloaded from NSRDB (Sengupta et al., 2018) database for the US and India based locations, and the PVGIS-SARAH (Huld et al., 2012) database was used for locations in Europe and Africa. TMY data provides the hourly values of direct normal solar irradiance (DNI, in W/m^2), ambient temperature (T_{amb}, in °C), and wind speed (v_w, in m/s), for each day of the year

2.2. Field Optical Losses and Optical Efficiency

The model developed in SAM takes determines the optical efficiency of parabolic trough solar collectors by taking into account both the losses that are a function of solar position as well as fixed loss multipliers. These fixed losses include tracking error (η_{track}), geometry defects (η_{geo}), mirror reflectance (ρ_M), dust on the envelope from mirror soiling (f_{dust}), concentration factor (f_{conc}), and solar field availability (f_{avail}). The multipliers used for these losses assume Solargenix SGX-1 solar collector and are provided in Table 1 below.

Table 1: Fixed loss multipliers for Solargenix SGX-1 solar collector used in CSP model					
η_{track}	η_{geo}	ρ_M	f_{dust}	f_{conc}	f_{avail}
0.994	0.98	0.935	0.98	1.0	0.99

For greater detail on each of these losses, we refer the readers to SAM technical manual (Michael J. and Gilman, 2011). The overall optical efficiency, η_{opt}, of the parabolic trough collectors is calculated as:

$$\eta_{opt} = \eta_{IAM}(\theta) \times \eta_{track} \times \eta_{geo} \times \rho_M \times \eta_{soil} \times f_{dust} \times f_{conc} \times f_{avail} \times \eta_{opt_HCE} \quad (1)$$

In the above equation, $\eta_{IAM}(\theta)$ is the incidence angle modifier that accounts for losses that are a function of solar position, as well as collector aperture foreshortening, glass envelope transmittance, selective surface absorption. Equation (2) provides the empirical formula for calculating $\eta_{IAM}(\theta)$ (Wagner and Gilman, 2011). The coefficients a_0, a_1, and a_2 used in this work were obtained from the SAM library and correspond to the Solargenix SGX-1 solar collector assemblies (SCA) with $a_0 = 1.0$, $a_1 = 0.0506$, and $a_2 = -0.1763$ respectively.

$$\eta_{IAM}(\theta) = a_0 + a_1 \frac{\theta}{cos(\theta)} + a_2 \frac{\theta^2}{cos(\theta)} \quad (2)$$

η_{opt_HCE} is the optical efficiency of heat collecting elements (HCEs). This term accounts for the HCE optical losses due to the different states that the receivers might be in. In this work, the model is built for 2008 Schott PTR70 HCE receivers, with field assumptions that 98.5% of the HCEs are assumed to be working as designed, 1% are assumed to have a glass-to-metal seal compromised, and remaining 0.5% are assumed to have the glass tube broken (resulting in an increased heat transfer between tube and atmosphere). These varied states result in some differences in the heat lost to atmosphere from the HCEs (refer section 2.3), and also the efficiency with which HCEs receive solar flux. η_{opt_HCE} is calculated by taking a summation of the impact

of bellows shadowing ($f_{bellows}$), envelope transmittivity (τ_e), and absorber absorption (α_a) over the percentage field fraction of each state the receivers are in as follows:

$$\eta_{opt_HCE} = \sum_{i=state} f_{bellows,i}\, \tau_{e,i}\, \alpha_{a,i}\ field_fraction_i \tag{3}$$

The multipliers for each of the three different states for HCEs are provided in Table 2:

Table 2: 2008 Schott PTR70 HCE optical efficiency coefficients for different receiver states

	Vacuum	Lost Vacuum	Broken Glass
$f_{bellows}$	0.963	0.963	0.963
τ_e	0.963	0.963	1.0
α_a	0.96	0.96	0.8

2.3. Field heat losses and net thermal power output

Thermal losses in CSP plant have a significant impact on the total power output of the plant, and therefore need to be modeled as accurately as possible. Field losses in a CSP plant are primarily comprised of piping heat losses from the flow of heat transfer fluid (HTF) in the pipes across the solar field, and heat losses in the HCEs. In this work, we use the empirical results obtained by NREL through heat-loss testing of 2008 Schott PTR70 HCE receivers (Burkholder and Kutscher, 2009). We define HCE losses as a function of T_{amb}, v_w, and DNI. The average integrated heat loss (Q_{HCEHL}) in W/m is given by:

$$Q_{HCEHL} = (Q_{HCEHL1} + Q_{HCEHL2} + Q_{HCEHL3} + Q_{HCEHL4}) \cdot F_{HeatLoss} \tag{4}$$

$$Q_{HCEHL1} = F_{HL_A0} + F_{HL_A5} \cdot \sqrt{v_w} \tag{5}$$

$$Q_{HCEHL2} = \left(F_{HL_A1} + F_{HL_A6} \cdot \sqrt{v_w}\right) \cdot \frac{T_{SF_out} + T_{SF_in} - T_{amb}}{2} \tag{6}$$

$$Q_{HCEHL3} = \left(F_{HL_A2} + F_{HL_A4} \cdot Q_{DNI}\right) \cdot \frac{T_{SF_out}^2 + T_{SF_out} \cdot T_{SF_in} + T_{SF_in}^2}{3} \quad (7)$$

$$Q_{HCEHL4} = F_{HL_A3} \cdot \frac{\left(T_{SF_out}^2 + T_{SF_in}^2\right) \cdot \left(T_{SF_out} + T_{SF_in}\right)}{4} \quad (8)$$

T_{SF_out} and T_{SF_in} are the solar field HCE receiver tube inlet and outlet temperatures. We assume Therminol VP-1 as the HTF and therefore T_{SF_in} and T_{SF_out} are kept fixed within the temperature limits of the vapor phase temperature limits for Therminol VP-1(Eastman, n.d.). More specifically, the HTF inlet and outlet temperatures are 293°C and 393°C respectively. These values are also used as the design-point conditions for the basis Rankine cycle in SAM technical manual. The coefficients used in the equations (4) to (8) are obtained from SAM and provided in Appendix A.

Similar to the calculation of HCE optical efficiency, equations (4) to (8) are applied to each state of the HCE receivers and summed over the states to calculate the total HCE heat losses (W/m^2) with the length of the SCAs (L_{SCA}) assumed to be 100 m:

$$Q_{HCE_loss} = \left(\sum_{i=state} Q_{HCEHL,i} \cdot field_fraction_i\right) \cdot \frac{L_{SCA}}{A_{aperture}} \quad (9)$$

Besides the heat loss in the receivers, there is some heat loss to the atmosphere as the HTF fluid circulates through pipes connecting different components in the CSP plant. These losses are calculated using an empirical equation developed by Patnode et al. (Patnode, 2006) with some minor modifications as indicated in SAM technical manual. The coefficients used in the equation (10) are obtained from SAM and provided in Appendix A, and $Q_{PHL_DesignT}$ is the piping heat loss at the CSP design point temperature:

$$Q_{pipe_loss} = \left(F_{PHL_A1}\Delta T + F_{PHL_A2}\Delta T^2 + F_{PHL_A3}\Delta T^3\right) \cdot Q_{PHL_DesignT} \cdot A_{aperture} \quad (10)$$

$$\Delta T = T_{avg} - T_{amb} \quad (11)$$

$$T_{avg} = \frac{T_{SF_out} + T_{SF_in}}{2} \quad (12)$$

The solar flux delivered to the CSP HCE, referred to as DNI_{norm} in this work, can be calculated from the hourly solar flux obtained from the meteorological data and the optical efficiency of the parabolic trough collectors:

$$DNI_{norm} = DNI \cdot \eta_{opt} \quad (13)$$

The total solar field thermal power output can then be calculated from the total solar field aperture area and the normalized DNI as:

$$Q_{thermal} = DNI_{norm} \cdot A_{aperture} \quad (14)$$

Building off of the general assumption that CSP systems are economical only for locations with DNI above 1800 kWh/(m^2yr), we use an average hourly minimum DNI_{norm} requirement of 200 W/m^2 before the plant can be assumed to operate on part/full load (Bishoyi and Sudhakar, 2017; Kaygusuz, 2011). As such, during the hours when the DNI_{norm} is below the minimum required DNI_{norm}, it is assumed that no heat is absorbed by the HCEs. Furthermore, due to the non-operational condition of the plant during the said hours, any HCE and piping losses are also ignored. The net thermal power output of the solar field can therefore be calculated as:

$$Q_{Net} = Q_{thermal} - Q_{HCE_{loss}} - Q_{pipe_loss} \quad (15)$$

2.4. Power block calculations

Given that the focus of the work is to highlight the potential enhancements to a CSP plant by hybridizing it with PV arrays, we bypass the calculation of hourly temperature of the HTF, and instead use a coefficient based equation that determines the cycle thermal to electric efficiency for the concentrated solar power plant based on the thermal cycle part load at any hour, as described in the SAM model. A non-dimensional gross cycle output ($\overline{\dot{W}_{gr}}$) is calculated using the ratio of

calculated thermal energy delivered to the power block ($\dot{Q_{pb}}$) and the design cycle thermal energy input to the turbine ($\dot{Q_{design}}$) as follow:

$$\overline{\dot{Q_{pb}}} = \frac{\dot{Q_{pb}}}{\dot{Q_{design}}} \tag{16}$$

$$\overline{\dot{W_{gr}}} = F_0 + F_1 \cdot \overline{\dot{Q_{pb}}} + F_2 \cdot \overline{\dot{Q_{pb}}}^2 + F_3 \cdot \overline{\dot{Q_{pb}}}^3 + F_4 \cdot \overline{\dot{Q_{pb}}}^4 \tag{17}$$

Where the coefficients $F_0 - F_4$ are obtained from SAM library assuming a dry cooled 80MWe SEGS turbine, and are provided in Table 3 below:

Table 3: Coefficients for calculating cycle thermal to electric efficiency for 80 MWe SEGS turbine

F_0	F_1	F_2	F_3	F_4
-0.037726	1.0062	0.076316	-0.044775	0.0

The net cycle power output from the power block was subsequently calculated as:

$$\dot{W}_{net} = 0.9 \times \overline{\dot{W}_{gr}} \cdot \dot{W}_{gr,design} \cdot \left(1 - F_{constant_loss}\right) \tag{18}$$

Here $F_{constant_loss}$ is a loss term incorporated in the SAM model to account for the losses that prevent the system from operating as designed. These losses include partial or complete system outages for maintenance, as well as any forced outages due to grid constraints, or other unplanned situations and are assumed to be 4%. Additionally, it is assumed that the net power generated by the power block is 90% of the design power output of the power block.

Similar to minimum DNI requirements for operation of the plant, real plants also experience high solar radiation conditions that can result is HTF temperatures much higher than the design values. In such situations, a number of collectors within a loop are deliberately de-focused to control the HTF loop outlet temperatures. We account for this real-world control effect by applying

an upper limit to the hourly power that can be generated from the CSP plant, set to the design turbine net power output.

2.5. Parasitic losses

Similar to field thermal losses, parasitic losses also have a major impact on the overall plant performance and can be as much as 10-15% of the gross electric output of the CSP plant. However, unlike thermal losses, parasitic losses refer to the electrical power required to run the critical components in the power system such as drive motors, electronic circuits, and pump motors. More specifically, we have taken into account the electrical losses from electric or hydraulic SCA drives that position the collector to track the sun ($P_{loss,SCA}$), electrical losses from cold HTF pumping in the solar field ($P_{loss,HTFpump}$), electrical losses from HTF pump operation to prevent the HTF from freezing ($P_{loss,Antifreeze}$), fixed losses from the power block ($P_{loss,PB}$), electrical losses from the balance of plant ($P_{loss,BoP}$), and electrical usage from operating the cooling towers ($P_{loss,CT}$). The CSP plants considered in this work do not have a thermal energy storage system and are also assumed to not have an auxiliary heater and boiler. As such, the parasitic losses from these last two systems is not modeled. To model parasitic losses, we use coefficient-based equations as used in SAM.

$$P_{loss,system} = P_{loss,system\ design} \cdot \left[F_0 - F_1 \frac{Q_{Net}}{Q_{SF,design}} + F_2 \left(\frac{Q_{Net}}{Q_{SF,design}} \right)^2 \right] \quad (19)$$

Here $Q_{SF,design}$ is the design solar field thermal energy, $F_0 - F_2$ are the coefficients obtained from SAM for SEGS VIII as a reference, and $P_{loss,system\ design}$ is the maximum value or the design point value of the parasitic loss for the system evaluated. The calculation of design point values is explained in great detail in the SAM documentation. Equation (19) is used for calculating the HTF pump losses and the Balance of Plant losses only, with $P_{loss,HTFpump}$ doubled in the CSP-

PV hybrid systems due to additional cooling requirements for the PV modules. The coefficients used for these losses are provided in Appendix A. $P_{loss,SCA}$ is calculated using Equation (20) where SCA_{factor} is the MWe power required per unit field aperture area and is assumed to be 2.66e-07 MWe/m^2.

$$P_{loss,SCA} = SCA_{factor} \cdot A_{aperture} \cdot Load\ Factor_{SCA} \quad (20)$$

$P_{loss,CT}$ is modeled slightly differently compared to the losses described above. It is modeled as either 50% or 100% of the cooling tower design losses depending on the plant load factor. Lastly, $P_{loss,antifreeze}$ and $P_{loss,PB}$ are modeled as 10% of $P_{loss,SCA}$ and 0.55% of the gross turbine power output respectively. It must be noted here that the anti-freeze pump is operational only when the solar field load is zero, i.e., the plant is not operating. Furthermore, all other losses with the exception of $P_{loss,PB}$ are assumed to be zero when the plant is not operating.

The net electrical power generated from the plant is the difference between power block power output and the parasitic losses.

3. CSP-PV Hybrid Plant Model

The hybrid retrofit system uses the design proposed in previous work (T Otanicar et al., 2018) based on a retrofit that installs a beam splitting dichroic mirror in the flux line between the primary mirror and the HCE. As can be seen in Figure 2 the dichroic mirror reflects a portion of the spectrum to the PV receiver (PVR) while transmitting the remaining flux to the original HCE element on the existing parabolic trough. The proposed retrofit utilizes high efficiency monocrystalline silicon solar cells, SunPower MAXEON cells were used in prior experiments. This retrofit approach allows for the overall width of the dichroic mirror to be changed (see Figure 2) to intercept lesser or greater fractions of the reflected light from the primary.

The hybrid plant model builds upon the CSP plant model by incorporating three major modifications. First, the optical properties of the dichroic mirrors must be determined such that the flux to CSP HCE and PVR can be determined. Second, the reduced flux to the CSP HCEs must be considered. Third, the electrical power output from the PVR needs to be determined. For the determination of the power output, a geometric concentration ratio of 30.2 is assumed (Otanicar et al., 2011). Each of these three components is discussed in detail below and can be seen in the modified simulation framework in Figure 3.

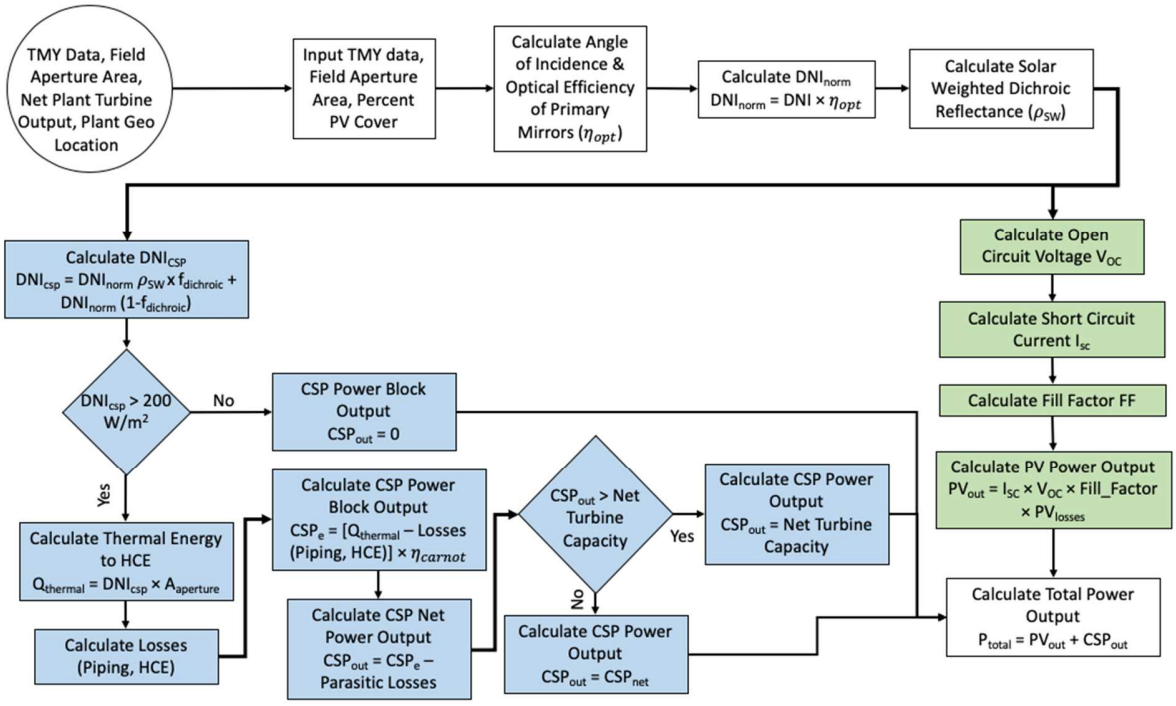

Figure 3: Framework of hourly simulation of hybrid CSP-PV retrofit collector for existing parabolic trough style powerplants.

3.1. Dichroic Mirror Properties

Dichroic mirrors are typically composed of highly controlled thicknesses of differing materials to achieve the desired wavelengths of transmission/reflection. A number of previous works have looked at optimization of potential filters for hybrid PV/T applications (Bierman et al.,

2016; Brekke et al., 2016; Orosz et al., 2016b) and is not considered here. It should be noted that the wavelengths selected depend upon both PV cell bandgap and operating temperature of the thermal receiver. Here, a dichroic mirror coating provided by Deposition Sciences Inc. for use with silicon PV cells and conventional parabolic trough powerplants, see Figure 4 for the spectral transmission and reflection as measured by the manufacturer.

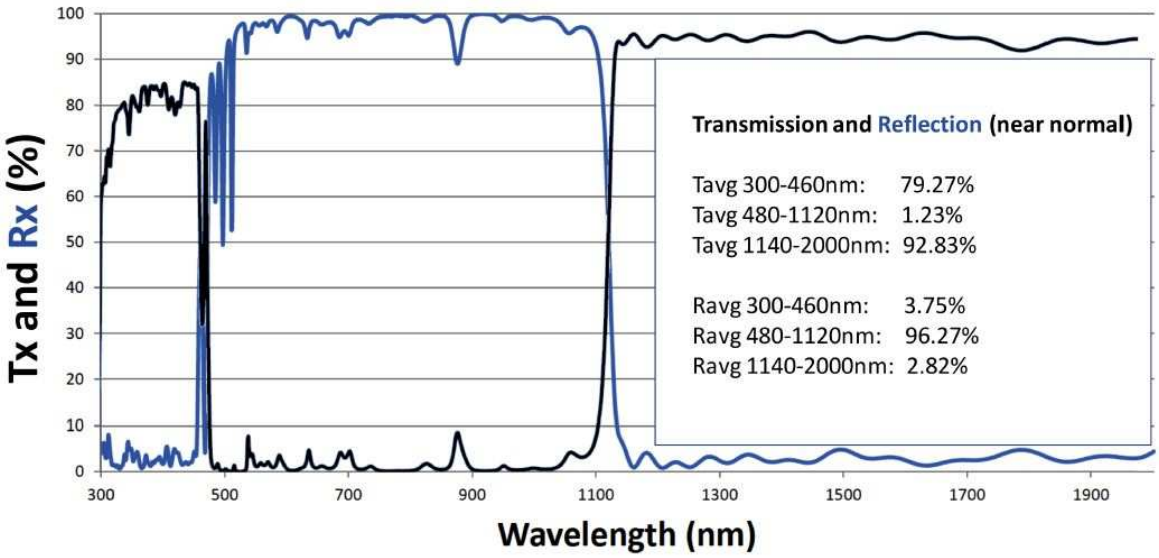

Figure 4**:** Measured spectral transmittance (Tx) and reflectance (Rx) (near normal) for the dichroic mirrors supplied by Deposition Sciences.

Using this data, the first step in the hybrid model is to calculate the solar weighted reflectance, as outlined below(Otanicar et al., 2009):

$$\rho_{sw} = \frac{\int_0^\infty R_x E_\lambda d\lambda}{\int_0^\infty E_\lambda d\lambda} \tag{21}$$

Knowing the solar weighted reflectance, the normalized DNI (including losses on the primary mirrors) can be used to find the solar flux component that would be directed to the PVR and the HCE respectively.

3.2. Modified Solar Flux to the CSP HCE

The solar flux delivered to the CSP HCE is modified by the inclusion of the retrofit through two main ways. First, the dichroic mirror intercepts a portion of the reflected sunlight based on the overall width of the mirror, see Figure 2. This method allows for the mirror to be designed to intercept some fraction of the reflected flux line up to 100% of the flux line. The second way the flux to the HCE is impacted is from partial spectral transmission to the HCE based on the previously determined solar weighted reflectance. The total solar power incident at the HCE is then found through:

$$P_{inc,CSP} = DNI_{norm} A_{aperture} (1 - f_{dichroic} + f_{dichroic} \rho_{sw}) \quad (22)$$

Where $A_{aperture}$ is the solar field aperture areas, and $f_{dichroic}$ is the fraction of the flux line intercepted by the dichroic mirror of the retrofit. Using the updated total power incident on the HCE the electrical power output from the thermal portion of the plant follows the same calculation as the CSP model outlined in section 2.

3.3. Electrical Power Output from PV Receiver

The next major addition to the model for the hybrid system is to include hourly electrical power output calculations for the PVR that is installed as a retrofit to the existing CSP plant. This portion of the model calculates the baseline cell performance, particularly the short circuit current, open circuit voltage, and fill factor. The open circuit voltage for a typical cSi solar cell accounting for temperature can be found (Markvart, 2009) a simplification that allows for simple cell property knowledge:

$$V_{OC} = V_{oc,ref} \left[1 + \beta_{VOC} \left(T_{PV} - T_{ref}\right)\right] \quad (23)$$

Where $V_{oc,ref}$ is the cell open circuit voltage at the reference condition (0.635 V), β_{VOC} is the open circuit voltage temperature coefficient (-0.0035 1/K), T_{PV} is the estimated PV module temperature, and T_{ref} is the reference temperature (25 °C). Determining the short circuit current

is found through the following relationship which considers the cell external quantum efficiency, and the concentration ratio on the PVR:

$$I_{sc} = x_{coverage} \times A_{aperture} \times f_{dichroic} \times \eta_{opt,dichroic} \times \frac{DNI_{norm}}{DNI_{AM1.5}} q \int_0^{\infty} R_x EQE_\lambda \phi_\lambda d\lambda \quad (24)$$

Where $x_{coverage}$ is the fraction of the SCA length covered by the cells (0.92), $\eta_{opt,dichroic}$ is the optical efficiency of the dichroic secondary mirrors found in earlier modeling (92%), q is the electron charge, EQE_λ the spectral external quantum efficiency (see figure 5), $DNI_{AM1.5}$ is the standard DNI in the AM1.5D spectrum (900 W/m^2), and ϕ_λ is the spectral photon flux for the standard AM1.5D spectrum.

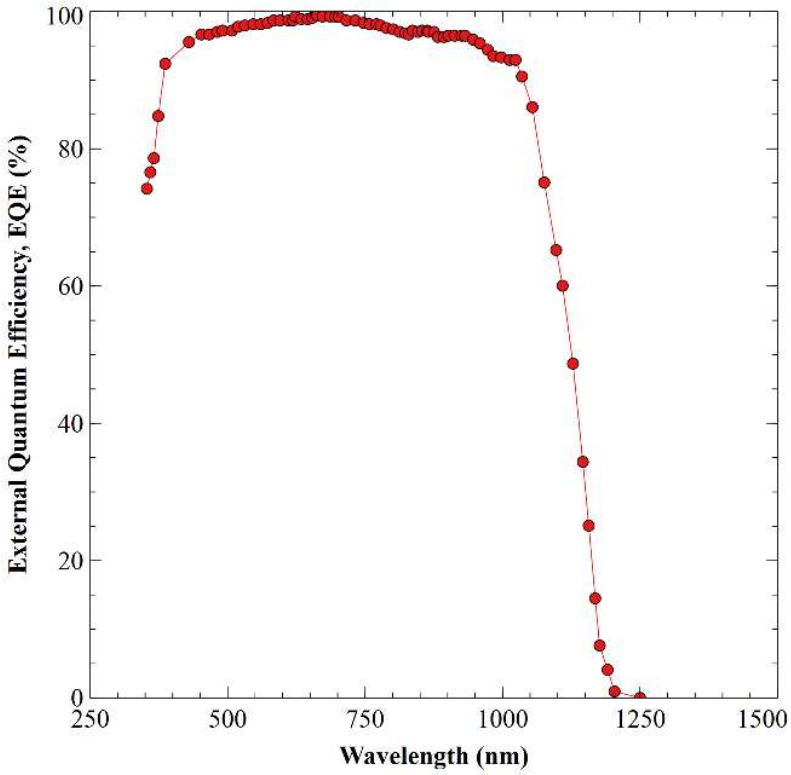

Figure 5**:** Spectral external quantum efficiency of the cSi cells analyzed in the PV receiver.

The fill factor is found using:

$$FF = FF_{ref}\left[1 + \beta_{FF}\left(T_{PV} - T_{ref}\right)\right] \quad (25)$$

Where FF_{ref} is the fill factor at the reference condition (0.79), and β_{FF} is the fill factor temperature coefficient found through the following relationship (Dupré et al., 2015):

$$\beta_{FF} = \beta_{P,max} - \beta_{VOC} - \beta_{JSC} \tag{26}$$

Where $\beta_{P,max}$ is the temperature coefficient of the maximum power point (-.0046 1/K), and β_{JSC} is the temperature coefficient of the short circuit current density, taken to be zero (Markvart, 2009). The total hourly electrical power output can be determined using the equation below taking into consideration losses from DC wiring, MPPT losses, and module mismatch.

$$PV_{out} = I_{sc}V_{oc}X_{losses}FF \tag{27}$$

$$X_{losses} = X_{DC-wiring}X_{MPPT}X_{module} \tag{28}$$

Where $X_{DC-wiring}$ is the losses associated with DC wiring of the module (0.99), X_{MPPT} the losses associated with the MPPT effectiveness (0.995), and X_{module} the derating for module mismatch along the SCA length (0.98). The total output electrical power output for each hourly simulation of the full retrofit is simply the sum of the PV receiver output and the CSP net power output:

$$P_{total} = PV_{out} + CSP_{out} \tag{29}$$

As mentioned in Section 2.5, for the hybrid model, the pumping losses for HTF are assumed to be twice as much as the CSP model to account for the additional pumping required to keep the PV cells cool.

3.4. Levelized Cost of Energy Calculation

To determine the feasibility of CSP-PV hybrid system, Levelized Cost of Energy (LCOE) was estimated using equation (30) (Ho et al., 2018). It is assumed that the cost of retrofit is driven exclusively by cost of PV cells and the existing capital cost is tied to the existing CSP plant.

$$LCOE = \frac{C_{CPV} + C_{inverter} + C_{O\&M} + C_{soft}}{E_{yearly}} * \frac{i(1+i)^n}{(1+i)^n - 1} \tag{30}$$

In the above equation, the interest rate (i) is assumed to be 8% (Ho et al., 2018), the number of years (n) is taken to be 25, and C_{CPV}, $C_{inverter}$, $C_{O\&M}$ and C_{soft} are the capital cost of the CPV retrofit, the inverter cost, the operations and maintenance cost of the plant and the costs associated with installation, developer cost, overhead etc., respectively. E_{yearly} is the estimated increase in yearly energy production.

$C_{inverter}$ is calculated from the maximum DC watts output from the PV retrofit assuming that the inverters will be sized based on the design PV output and C_{soft} is determined based on the maximum energy output from the PV retrofit in 1 year for 50% PV coverage area. It is subsequently assumed constant for other percentage PV coverage cases as labor and other costs should not change. 50% coverage case was selected as it was observed to be the most beneficial among the CSP plants analyzed in this work. Operation and Maintenance cost, $C_{O\&M}$, is based on inverter, module and component replacement only whereas all other costs are shared with the original CSP. The capital cost of the CPV receiver retrofit includes the cost of the PV cells as well as the cost of extrusion and the dichroic mirrors. The cost of the dichroic is based on the cost Low-emissivity glass, while the extrusion cost is based upon the cost of aluminum extrusion available online (Otanicar et al., 2020).

$$C_{CPV} = C_{cell} w_{PV} L_{SCA} + C_{extrusion} L_{SCA} + C_{dichroic} 2 L_{dichroic} L_{SCA} \quad (31)$$

where C_{cell} is the cell cost on a per unit area basis and w_{PV} is the width of PV cell. The assumed values of constants in (30) and (31) are provided in Table 4.

Table 4: Constants for LCoE Calculation.

Parameter	Value	Units	Source
$C_{inverter}$	0.06	\$/Wdc	(Fu et al., 2018)
$C_{O\&M}$	9.1	\$/kW/Yr	(Fu et al., 2018)
C_{soft}	0.41	\$/Wdc	(Fu et al., 2018)
w_{PV}	0.02	m	As built
$C_{dichroic}$	28	\$/m^2	Online prices
$C_{extrusion}$	18	\$/m	Online aluminum prices
C_{cell}	0.28	\$/W	(Woodhouse et al., 2019)
$L_{dichroic}$	0.2075	m	Assumed
i	8	%	(Ho et al., 2018)
n, number of years	25	Years	Assumed

4. Results and Discussion

4.1. CSP model validation

The simulations are carried out using the hourly meteorological data and the net power output is summed over an entire month before comparing the results with those obtained from SAM. For the purpose of validation of the CSP model, the Genesis Solar Energy Project was used as the reference plant with field aperture area of 1,928,320 m^2 and a net turbine power output of 250 MW. The standard length of each SCA is assumed to be 100m aligned parallel to the horizontal ($\theta_{col} = 0$) and the torque tube along the N-S axis ($\gamma_{col} = 0$). The results from the CSP model are validated against the simulation results obtained from SAM using 2017 meteorological data for the site as shown in Figure 6. The results are also compared with the actual energy generation on record for the power plant in 2017 ("EIA: Plant level data for Genesis Solar Energy Project," n.d.). For better comparison, it is noted that the results from the CSP model are comparable with those from both SAM as well as the actual generation on record for the months March through October.

Some deviations were observed over the winter months, for both the CSP model as well as SAM results. These deviations are primarily due to the fixed temperature assumption for the HTF fluid at the solar field inlet and outlet (Refer Section 2.3). Furthermore, the CSP model does not account for the additional heating that might be required to get the HTF fluids to the service temperature during the winter months resulting in lower parasitic losses. Per EIA, the overall net energy generated on record between March and October 2017 was 541,158 MWh for the Genesis Solar Energy Project. In comparison, the predicted net energy generation between the same months from CSP model and SAM are 551,197 MWh and 560,188 MWh respectively, which are both within 3.5% of the actual observed power generation. Based on the results in Figure 6 the CSP model is capable of providing a high-level prediction of plant level production from a parabolic trough CSP plant.

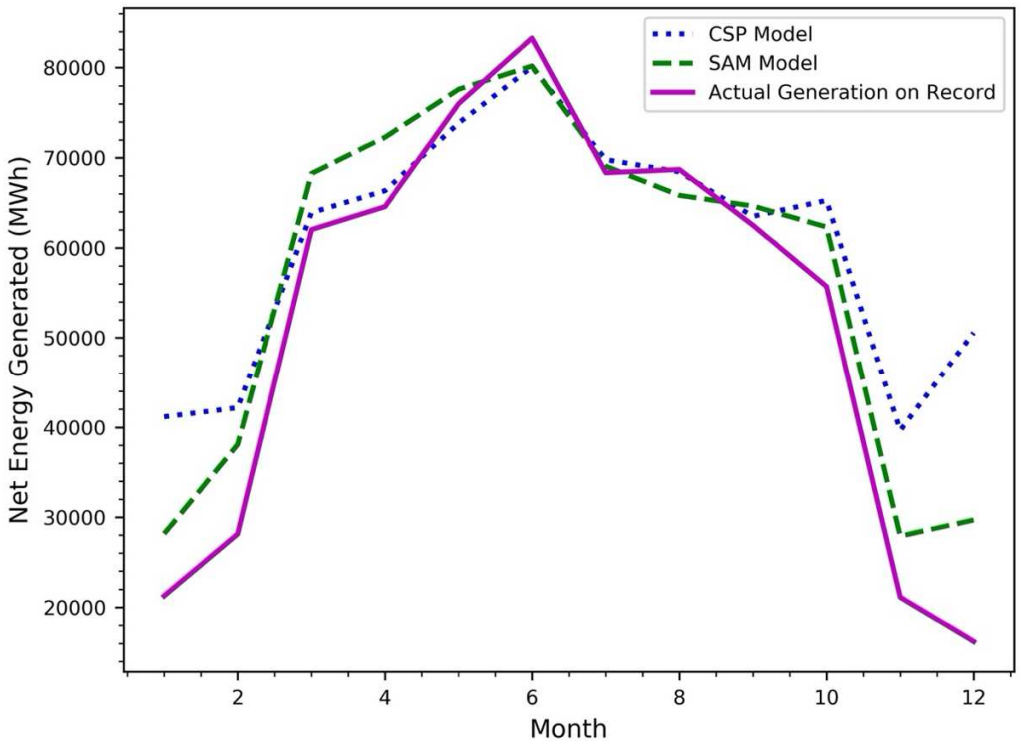

Figure 6: Net energy output from CSP model compared with those from SAM simulation and the actual generation on record for Genesis solar power project in 2017.

4.2. Simulation of Retrofitted CSP Plants

The CSP model was subsequently modified to include a PV retrofit. The starting assumption for the modeling of the PV retrofit simulation is that the dichroic covers 50% of the fluxline reflected by the primary optics ($f_{dichroic}$=0.5) with the optical properties outlined in Figure 4. The Genesis Solar Power project was again used as the reference plant, simulations for the hourly net power generated were run using the meteorological data from 2017. The hourly net energy generated was summed over each month to compare the net monthly energy generated as shown in Figure 7. For a value of $f_{dichroic}$=0.5, the retrofit model consistently indicated an increase in monthly net energy generated for the Genesis Solar Power project.

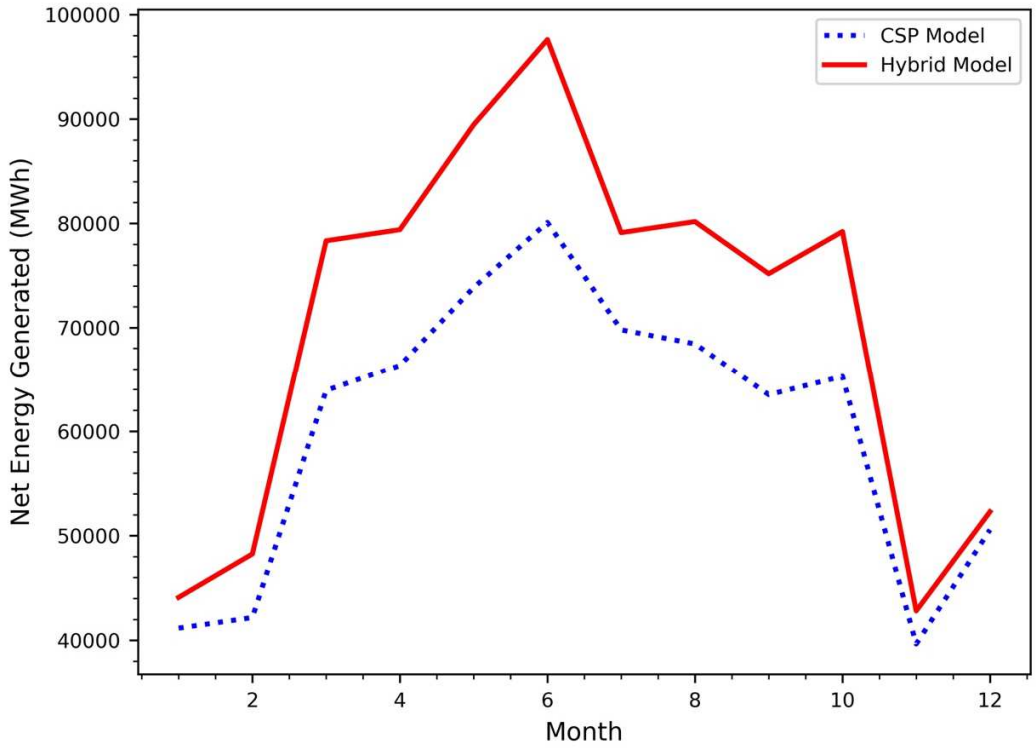

Figure 7: Comparison of net energy output from CSP model and CSP-PV hybrid model for Genesis solar power project in 2017.

The reasons for the increased electrical power output are two-fold. First, the efficiency of the PV cells under the resulting spectrum reflected from the dichroic is higher than that of the power

block. The second reason results from the operational constraints associated with a typical CSP facility: no output at low flux levels and defocusing of the mirrors during peak solar flux to not exceed the net power block output. While the original CSP model restricted the maximum net power generated to 250 MW for Genesis project (the net power block output) to reflect the defocusing that occurs in real facilities without thermal energy storage, this limitation only applies for the CSP component of the hybrid system whereas the PV component continued to generate power from the redirected flux from the dichroic mirrors. This results in a significant boost from the overall plant as defocusing is not required as the thermal load to the power block never exceeds the net power block design output and the PV can take what is normally excess power and generate electricity. Over the course of the year this results in 17% increase in the total electrical energy output. To better understand this reason for performance improvement, the energy generated from both the models was broken down into the gross CSP energy generated, parasitic losses, and the PV energy generated as shown in Figure 8.

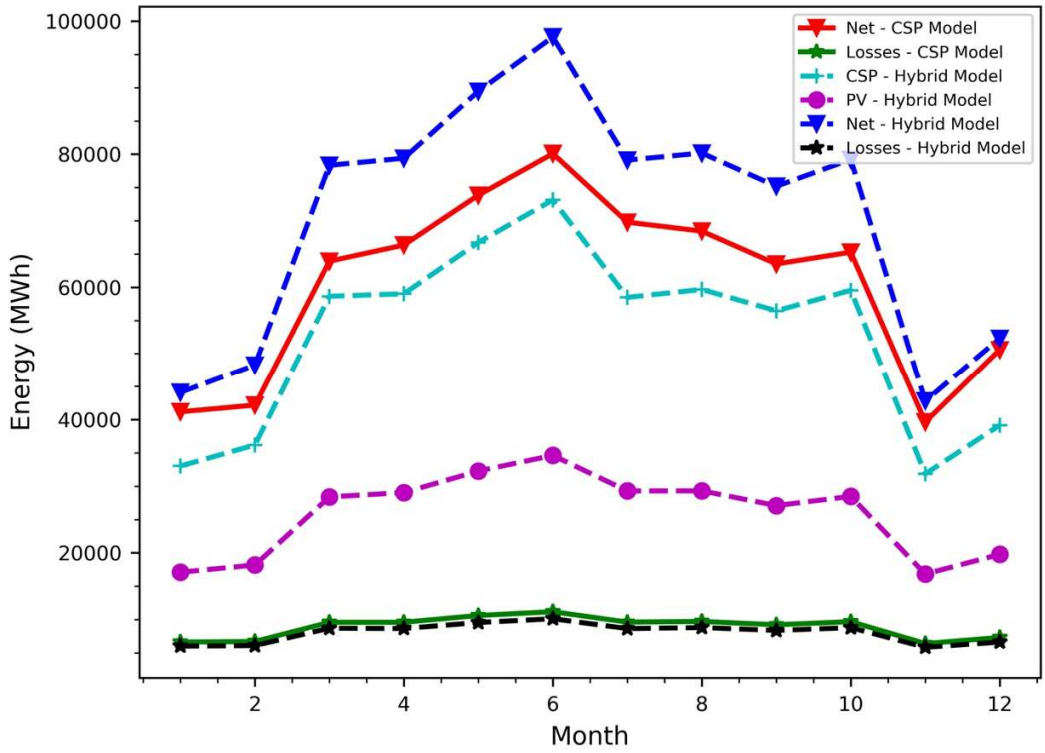

Figure 8: Comparison between different component of CSP model (solid lines) and CSP-PV hybrid model (dashed lines) for Genesis solar power project in 2017.

It was noted that due to reduction in total flux to the HCE in the hybrid model, the gross energy generated by the CSP component in the CSP-PV hybrid model was consistently lower than that in the CSP model. However, this also resulted in lower parasitic losses in the hybrid CSP-PV model as the parasitic losses were a function of the net solar field thermal energy available to the CSP component of the model. For the CSP Model, parasitic losses were calculated to be 14.7% of the annual net energy generated, whereas in the CSP-PV hybrid model, the parasitic losses dropped to 11.4% of the new annual net energy generated. While this is counterintuitive it is driven by the reduction in the parasitic losses to the CSP facility from substantial operation at part design thermal load. These effects combined with the additional power generated by the PV component in the hybrid model resulted in an overall increase in the net energy generated. It is also noted that with a value of $f_{dichroic}$=0.5, the net energy generated from the CSP component remained the dominant

source of energy for any given month. Figure 9 focuses on the results from the CSP-PV hybrid model with net energy output broken down into individual components. From Figure 9 it can be observed that in the summer months the CSP and PV electricity generated increases substantially, while the losses mainly remain nearly constant over the year in comparison to total energy production.

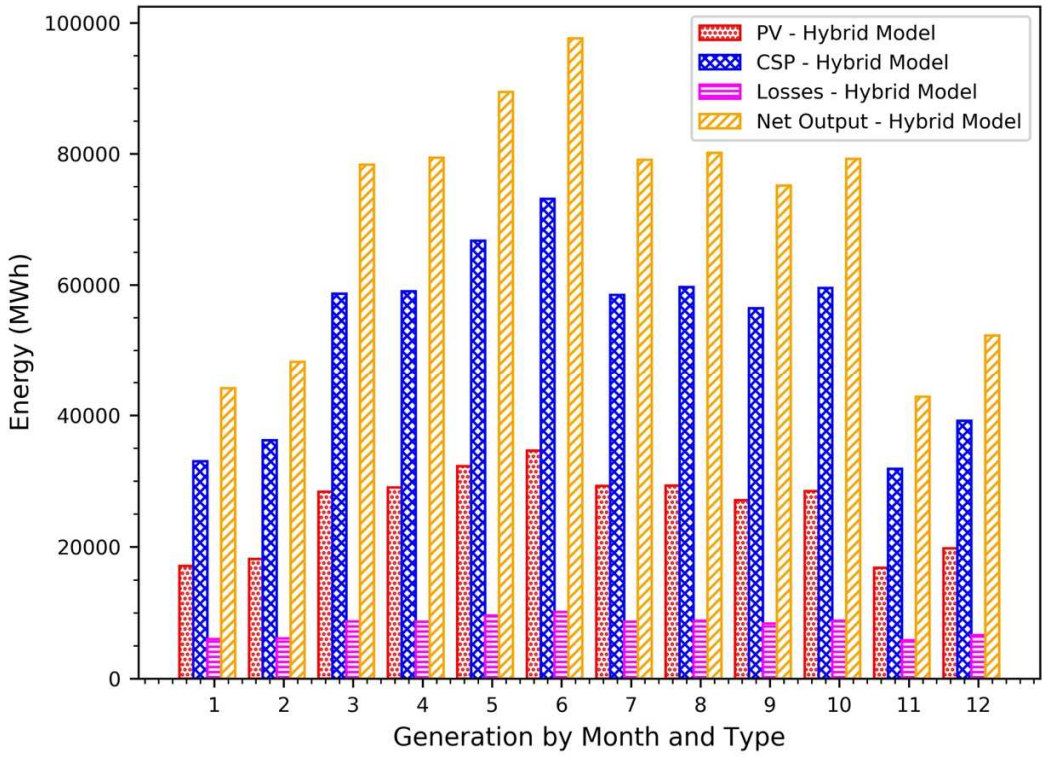

Figure 9: Individual contributions from the CSP and PV components of CSP-PV hybrid model for Genesis Solar Power project in 2017.

In order to further understand the behavior of the hybrid CSP-PV model, the energy generated for the summer and winter solstices are compared. Figure 10 and Figure 11 show the breakdown between the CSP and PV components (stacked together to show the total energy output) for the CSP-PV hybrid model, and the CSP only model for summer and winter solstice in 2017 respectively. It can be seen in Figure 10 that for the peak sun hours on the summer solstice, the net energy generation from CSP system is limited to the net energy generation to the turbine net

capacity to reflect system defocus during high solar flux hours resulting in lost energy. Conversely, the CSP component of CSP-PV hybrid model does not reach the peak capacity at any of those hours and is still generating an average 200 MW power. Additionally, the power generated from the PV component pushes the total electrical energy generated from the hybrid plant by nearly 20%. In the early morning hours and late afternoon, the CSP model typically outperforms the CSP-PV hybrid model.

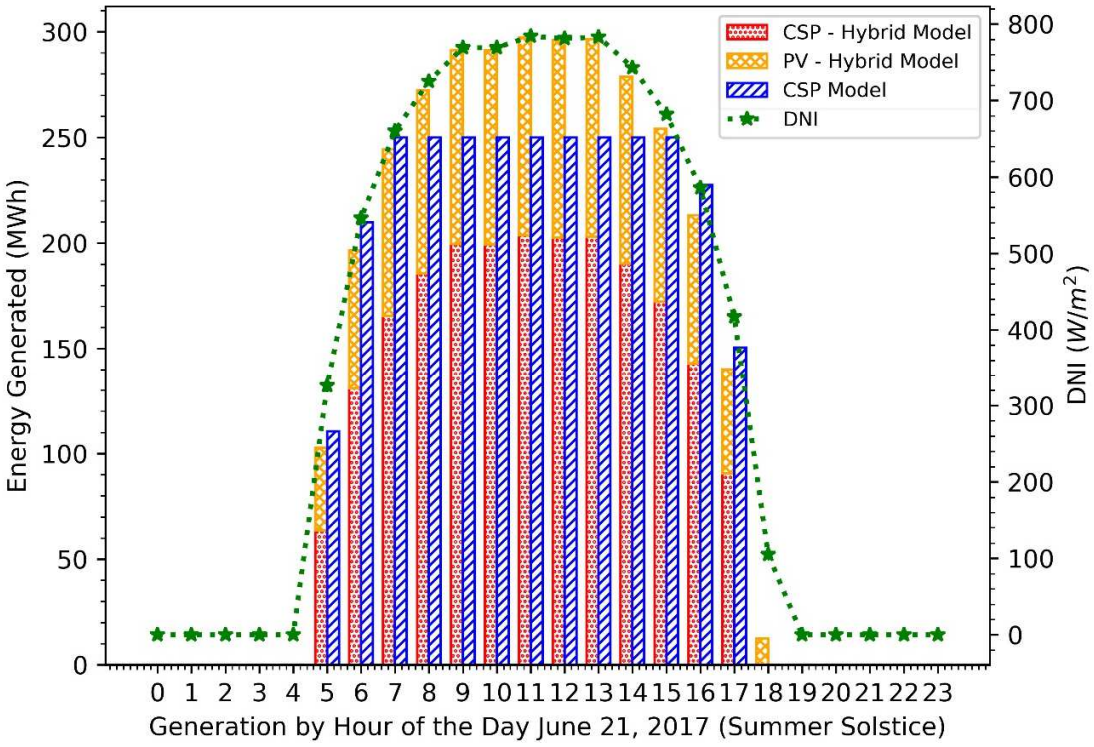

Figure 10: Hourly energy generation breakdown between CSP and PV components in CSP-PV hybrid model for Summer Solstice 2017.

On the winter solstice, see Figure 11, it is noted that the minimum DNI requirement is met for fewer hours during the day, and observations from the summer solstice day continue to hold during the wintertime as well.

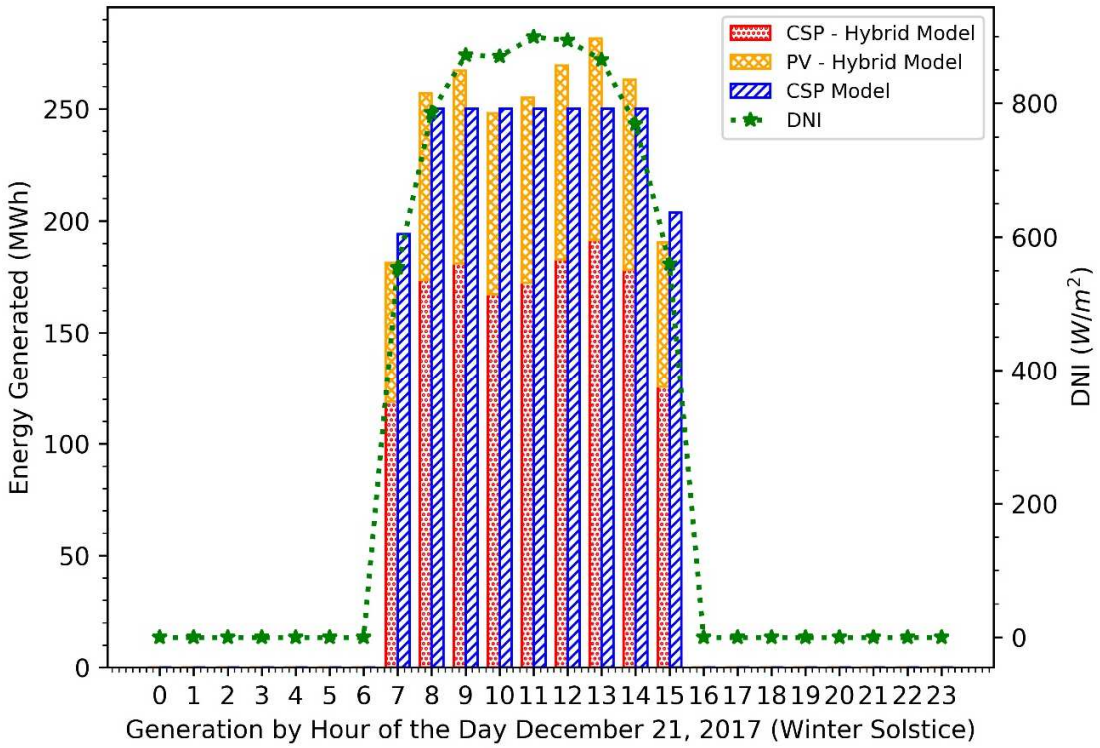

Figure 11: Hourly energy generation breakdown between CSP and PV components in CSP-PV hybrid model for Winter Solstice 2017.

4.3. Effect of solar multiple

To determine the full potential of the hybrid retrofit on parabolic trough powerplants, the previously validated hybrid CSP-PV model was used to simulate hourly performance across a full year for existing operational parabolic trough powerplants using RP-3 mirrors. Plants with RP-3 mirrors were selected as the designed optical platform was designed for the focal point of RP-3 mirrors as well as the fact that of the 3.62 GW of installed CSP capacity 66% is comprised of RP-3 primary mirrors (National Renewable Energy Laboratory, 2017). Seven different CSP plants without thermal energy storage were picked from different geographical locations and the hourly meteorological data for these locations for the year 2014 was used for the analysis. Furthermore, the simulations were conducted at dichroic intercept fractions of $f_{dichroic}$= 25%, 50%, and 75%. The selected plants for simulation are provided in Table 5.

Table 5: List of parabolic trough CSP plants evaluated using CSP-PV hybrid model

Plant Name	**Location**	**Aperture Area (m^2)**	**Net Turbine Capacity (MW)**	**Solar Multiple**	**$DNI_{Average}$ (kWh/m2-Day)**
ISCC Ain Beni Mathar	Ain Beni Mathar, Morocco	183,120	20	2.26	6.36
Solacor 1	El Carpio Córdoba, Spain	300,000	50	1.48	5.93
Godavari Solar Project	Nokh, Rajasthan, India	392,400	50	1.93	4.71
Solar Electric Generating Station VIII (SEGS VIII)	Harper Dry Lake, California	464,340	80	1.43	8.02
Shams 1	United Arab Emirates	627,840	100	1.55	6.63
Genesis Solar Energy Project	Blythe, California	1,928,320	250	1.9	7.63
Mojave Solar Project	Harper Dry Lake, California	1,559,347	250	1.54	8.02

In the Table above, solar multiple is calculated by assuming a design DNI of 1000 W/m^2, design field solar thermal efficiency ($\eta_{solar\ thermal,design}$) of 73%, and a design cycle thermal efficiency ($\eta_{cycle,design}$) of 33.74%, as follows:

$$Solar\ Multiple\ (SM) = \frac{DNI_{design} \cdot A_{aperture} \cdot \eta_{cycle,design} \cdot \eta_{solar\ thermal,design}}{\dot{W}_{net}} \quad (32)$$

The results from the simulations for the different plants and corresponding solar multiples as shown in Figure 12. As can be seen, CSP plants with a solar multiple of 1.6 or less, an increase in $f_{dichroic}$ lowers the net electrical energy generated. In some cases, for low values of solar multiple the installation of the PV retrofit is detrimental to the plant. At low values of solar multiple (less than 1.6) the percent change in electrical energy output varies from -10 to 6%. At solar multiples

exceeding 1.6 the increase in overall electrical energy output from the plan ranges from 10% to greater than 27%. An exception is observed for the Godavari Solar Project, where despite a solar multiple of 1.96, a decrease in net energy generated is observed from the CSP-PV hybrid model. Upon further comparison, it is seen that the average daily DNI for Nokh, Rajasthan, India (location for Godavari Solar Project) is only 4.71 kWh/m^2-Day compared to 7.63 kWh/m^2-Day for Genesis Solar Energy Project that has a similar solar multiple of 1.9 (Refer Table 5). Furthermore, while the benefits for installing PV retrofit on plants with solar multiple greater than 1.6 are evident from Figure 12, it is also important to note that a balance must be maintained between the percentage aperture area covered by the PV retrofit as the gain in annual energy generated appears to decline as the coverage area increases from 75% to 100%. It must be noted that the case with 100% PV coverage area is also a CSP-PV hybrid plant where a small fraction of incident solar flux, that is not reflected by the dichroic mirrors, goes to the CSP component.

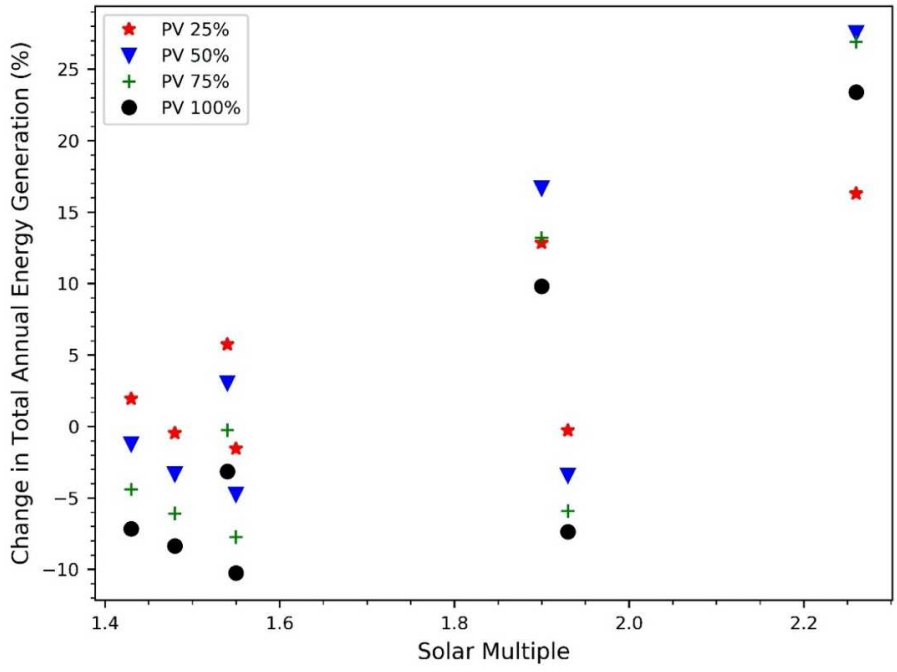

Figure 12: Change in annual energy generated for different CSP plants across the globe plotted against corresponding solar multiple and different PV coverage area.

LCOE calculations were done for the different PV coverage area percentage using the values identified in Table 4. It was observed that the LCOE for genesis plant decreased as the PV coverage increased from 25% to 50% and subsequently started rising again with further increase in PV coverage, driven by the cell cost and dichroic mirror cost. If the retrofit provided no increase in plant output, the LCOE was not calculated as there would be no benefit (NB). The results from LCOE calculation are summarized in Table 6. As can be seen the minimum LCOE occurs near the 50% coverage case at a LCOE of ~$0.07/kWh. Reductions in cell costs and dichroic mirror costs could lead to substantial LCOE reductions.

Table 6: LCOE for different percentage PV coverage of parabolic trough CSP plants evaluated using CSP-PV hybrid model (NB- No benefit)

Solar Multiple	Percentage PV Coverage			
	25%	50%	75%	100%
1.9	$0.094	$0.078	$0.103	$0.143
1.54	$0.190	$0.381	NB	NB
1.43	$0.543	NB	NB	NB
1.93	NB	NB	NB	NB
2.26	$0.113	$0.074	$0.083	$0.105
1.48	NB	NB	NB	NB

To illustrate the potential impact of a hybrid CSP-PV system retrofit in the field, the current total installed capacity for RP-3 parabolic trough CSP plants without thermal storage for different solar multiples is presented in Figure 13. The majority of the CSP installed capacity is around a solar multiple of 1.4 – 1.5, likely meaning that only small gains in annual energy output could be achieved for those plants. Figure 12 also indicates that the retrofit hybridization needs to be

considered on a plant-by-plant basis to fully understand the interaction of the existing plant design, plant location, and retrofit design on overall plant operation.

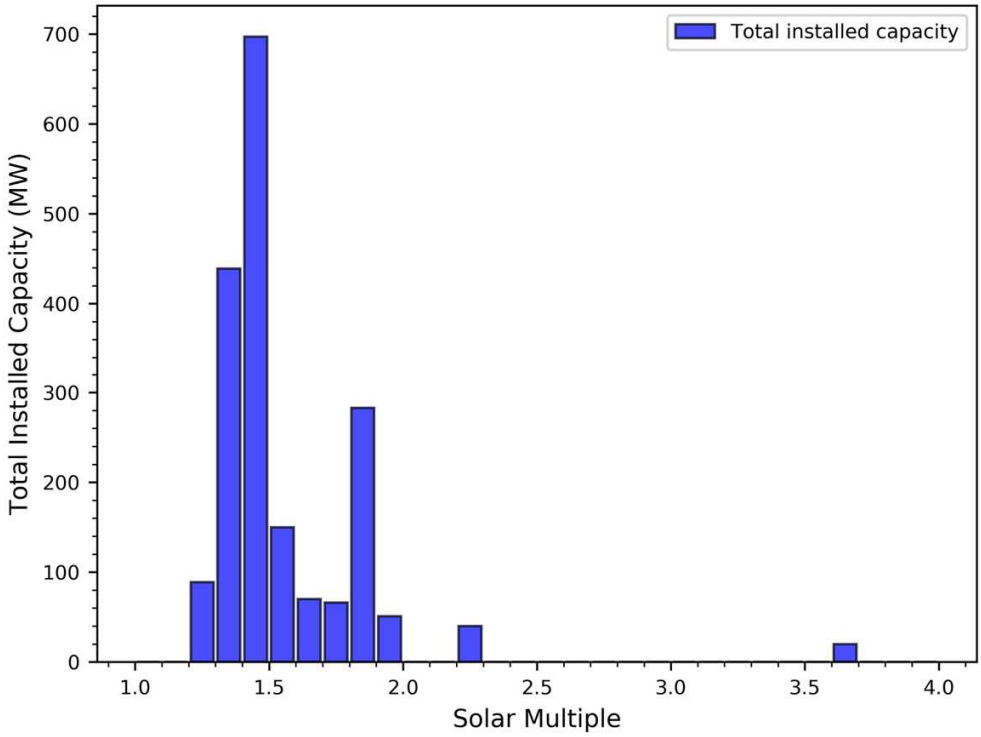

Figure 13: Current total installed capacity for CSP plants using RP-3 parabolic troughs and no thermal storage.

5. Conclusions

This work develops a modeling framework for analyzing concentrating solar thermal power and photovoltaic hybrids at the plant level over an entire year. The model builds upon the existing and well validated System Advisor Model with modifications to handle the spectral beam splitting and the addition of a photovoltaic receiver. The concentrating solar power portion of the model is validated against SAM and actual data for the Genesis Solar Power project on record. While from March through October the results from CSP code are within 1.8% and 1.6% of the electrical energy output from actual data on record and SAM respectively, the model overpredicts by 15.4%

and 5.9% respectively over the course of the entire year. Adding the proposed retrofit to the same powerplant with 50% intercept fraction by the dichroic mirrors results in an increased yearly electrical energy output of 16.7% compared to that from the CSP model. Further investigation demonstrates that the majority of the increase is the result of not requiring the total plant to defocus when the thermal output exceeds the net power block output, in the absence of any thermal storage. To further demonstrate the role of excess solar power, the model was used to simulate 6 additional existing concentrating solar power plants with various geographic locations and with varied levels of solar multiples. Results indicated that higher levels of solar multiple resulted in an increased amount of electrical energy production when a system level retrofit, up to a 30% increase. In general, the magnitude of the increase is also tied to the fraction of the original aperture that the dichroic intercepts. At low levels of solar multiple, less than 1.6, this effect is reversed, and the addition of the retrofit can be detrimental to plant performance. The LCOE of the retrofit in cases where an increase in yearly production was observed was minimized at the 50% coverage case, with an LCOE of ~$0.07/kWh. Future work should focus on the impact of a retrofit in the presence of thermal energy storage particularly where the excess thermal energy can be dispatched to the thermal storage and not capped because of thermal load exceeding net turbine capacity.

Declaration of Competing Interest

The authors declare no conflicts of interest.

Acknowledgements

The authors would like to acknowledge support from the U.S. Department of Energy ARPA-E FOCUS program under award number DE-AR0000729.

References

An, W., Li, J., Ni, J., Taylor, R.A., Zhu, T., 2017. Analysis of a temperature dependent optical window for nanofluid-based spectral splitting in PV/T power generation applications. Energy Convers. Manag. 151, 23–31. https://doi.org/10.1016/j.enconman.2017.08.080

Bierman, D.M., Lenert, A., Wang, E.N., 2016. Spectral splitting optimization for high-efficiency solar photovoltaic and thermal power generation. Appl. Phys. Lett. 109, 243904. https://doi.org/10.1063/1.4971309

Birol, F. (IEA), 2018. Renewables 2018: Market analysis and forecast from 2018 to 2023.

Bishoyi, D., Sudhakar, K., 2017. Modeling and performance simulation of 100 MW PTC based solar thermal power plant in Udaipur India. Case Stud. Therm. Eng. 10, 216–226. https://doi.org/10.1016/J.CSITE.2017.05.005

Branz, H.M., Regan, W., Gerst, K.J., Borak, J.B., Santori, E.A., 2015. Hybrid solar converters for maximum exergy and inexpensive dispatchable electricity. Energy Environ. Sci. https://doi.org/10.1039/C5EE01998B

Brekke, N., Otanicar, T., DeJarnette, D., Hari, P., 2016. A Parametric Investigation of a Concentrating Photovoltaic/Thermal System With Spectral Filtering Utilizing a Two-Dimensional Heat Transfer Model. J. Sol. Energy Eng. 138. https://doi.org/10.1115/1.4032452

Burkholder, F., Kutscher, C., 2009. Heat Loss Testing of Schott's 2008 PTR70 Parabolic Trough Receiver. Golden, CO (United States). https://doi.org/10.2172/1369635

Cocco, D., Migliari, L., Petrollese, M., 2016. A hybrid CSP–CPV system for improving the dispatchability of solar power plants. Energy Convers. Manag. 114, 312–323. https://doi.org/10.1016/j.enconman.2016.02.015

Crisostomo, F., Hjerrild, N., Mesgari, S., Li, Q., Taylor, R.A., 2017. A hybrid PV/T collector using spectrally selective absorbing nanofluids. Appl. Energy 193, 1–14. https://doi.org/10.1016/j.apenergy.2017.02.028

Dupré, O., Vaillon, R., Green, M.A., 2015. Physics of the temperature coefficients of solar cells. Sol. Energy Mater. Sol. Cells 140, 92–100. https://doi.org/10.1016/j.solmat.2015.03.025

Eastman, n.d. Technical Data Sheet Therminol® VP1 Heat Transfer Fluid [WWW Document]. URL https://productcatalog.eastman.com/tds/ProdDatasheet.aspx?product=71093459

EIA: Plant level data for Genesis Solar Energy Project [WWW Document], n.d.

Fisher, B., Biddle, J., 2011. Luminescent spectral splitting: Efficient spatial division of solar spectrum at low concentration. Sol. Energy Mater. Sol. Cells 95, 1741–1755. https://doi.org/10.1016/j.solmat.2011.01.043

Fu, R., Feldman, D.J., Margolis, R.M., 2018. U.S. Solar Photovoltaic System Cost Benchmark: Q1 2018. https://doi.org/10.2172/1483475

Goel, N., Taylor, R.A., Otanicar, T., 2020. A review of nanofluid-based direct absorption solar collectors: Design considerations and experiments with hybrid PV/Thermal and direct steam generation collectors. Renew. Energy 145, 903–913.

https://doi.org/10.1016/j.renene.2019.06.097

Ho, C.K., McPheeters, C.O., Sharps, P.R., 2018. Hybrid CSP/PV receivers: Converting optical spillage to electricity, in: AIP Conference Proceedings. American Institute of Physics Inc., p. 170006. https://doi.org/10.1063/1.5067170

Huld, T., Müller, R., Gambardella, A., 2012. A new solar radiation database for estimating PV performance in Europe and Africa. Sol. Energy 86, 1803–1815. https://doi.org/10.1016/J.SOLENER.2012.03.006

IRENA, 2012. Renewable Energy Technologies: Cost Analysis Series: Concentrating Solar Power (No. 2), Renewable Energy Technologies: Cost Analysis Series.

Kaygusuz, K., 2011. Prospect of concentrating solar power in Turkey: The sustainable future. Renew. Sustain. Energy Rev. 15, 808–814. https://doi.org/10.1016/J.RSER.2010.09.042

Markvart, T., 2009. Solar Electricity, 2nd ed. John Wiley & Sons, Ltd.

Michael J., W., Gilman, P., 2011. Technical manual for the SAM physical trough model, NREL Technical report. Golden, CO.

Moaleman, A., Kasaeian, A., Aramesh, M., Mahian, O., Sahota, L., Nath Tiwari, G., 2018. Simulation of the performance of a solar concentrating photovoltaic-thermal collector, applied in a combined cooling heating and power generation system. Energy Convers. Manag. 160, 191–208. https://doi.org/10.1016/j.enconman.2017.12.057

National Renewable Energy Laboratory, 2017. Concentrating Solar Power Projects - Parabolic Trough Projects | Concentrating Solar Power | NREL [WWW Document].

National Renewable Energy Laboratory, 2016. System Advisor Model Version 2016.3.14 (SAM 2016.3.14). National Renewable Energy Laboratory.

O'Hern, H., Orosz, M., Otanicar, T., 2018. Parabolic trough powerplants nearing PPA end: Retrofit or replace?, in: SolarPACES 2017. p. 030010. https://doi.org/10.1063/1.5067026

O'Hern, H., Otanicar, T., Orosz, M., 2017. Performance and economic optimization of hybrid solar thermal and photovoltaic power plants with dynamic simulation, in: 30th International Conference on Efficiency, Cost, Optimisation, Simulation and Environmental Impact of Energy Systems. San Diego, CA.

Orosz, M., 2015. Photovoltaics and concentrating solar power : why hybridization makes sense. SPIE Newsroom 1–4. https://doi.org/10.1117/2.1201508.006018

Orosz, M., Zweibaum, N., Lance, T., Ruiz, M., Morad, R., 2016a. Spectrum-splitting hybrid CSP-CPV solar energy system with standalone and parabolic trough plant retrofit applications, in: AIP Conference Proceedings. p. 070023. https://doi.org/10.1063/1.4949170

Orosz, M., Zweibaum, N., Lance, T., Ruiz, M., Morad, R., 2016b. Spectrum-Splitting Hybrid CSP-CPV Solar Energy System with Standalone and Parabolic Trough Plant Retrofit Applications, in: SolarPACES 2015. Johannesburg, South Africa.

Otanicar, Todd, Dale, J., Orosz, M., Brekke, N., DeJarnette, D., Tunkara, E., Roberts, K., Harikumar, P., 2018. Experimental evaluation of a prototype hybrid CPV/T system utilizing

a nanoparticle fluid absorber at elevated temperatures. Appl. Energy 228, 1531–1539. https://doi.org/10.1016/j.apenergy.2018.07.055

Otanicar, T, Orosz, M., Wingert, R., Yetter, K., McPheeters, C., Sharps, P., 2018. Design and Analysis of a CPV Retrofit for Parabolic Trough Powerplants, in: World Conference on Photovoltaic Energy Conversion 7-IEEE PVSC.

Otanicar, T.P., Chowdhury, I., Prasher, R., Phelan, P.E., 2011. Band-gap tuned direct absorption for a hybrid concentrating solar photovoltaic/thermal system. J. Sol. Energy Eng. Trans. ASME 133. https://doi.org/10.1115/1.4004708

Otanicar, T.P., Phelan, P.E., Golden, J.S., 2009. Optical properties of liquids for direct absorption solar thermal energy systems. Sol. Energy 83, 969–977. https://doi.org/10.1016/j.solener.2008.12.009

Otanicar, T.P., Wingert, R., Orosz, M., McPheeters, C., 2020. Concentrating photovoltaic retrofit for existing parabolic trough solar collectors: Design, experiments, and levelized cost of electricity. Appl. Energy 265, 114751. https://doi.org/10.1016/j.apenergy.2020.114751

Patnode, A.M., 2006. Simulation and performance evaluation of parabolic trough solar power plants.

Penn, I., 2017. Edison and Tesla unveil giant energy storage system [WWW Document]. Los Angeles Times.

Petrollese, M., Cocco, D., 2016. Optimal design of a hybrid CSP-PV plant for achieving the full dispatchability of solar energy power plants. Sol. Energy 137, 477–489. https://doi.org/10.1016/j.solener.2016.08.027

Robertson, J., Riggs, B., Islam, K., Ji, Y.V., Spitler, C.M., Gupta, N., Krut, D., Ermer, J., Miller, F., Codd, D., Escarra, M., 2019. Field testing of a spectrum-splitting transmissive concentrator photovoltaic module. Renew. Energy 139, 806–814. https://doi.org/10.1016/j.renene.2019.02.117

Sengupta, M., Xie, Y., Lopez, A., Habte, A., Maclaurin, G., Shelby, J., 2018. The National Solar Radiation Data Base (NSRDB). Renew. Sustain. Energy Rev. 89, 51–60. https://doi.org/10.1016/j.rser.2018.03.003

SolarPACES, 2019. Concentrating Solar Power Projects [WWW Document].

Starke, A.R., Cardemil, J.M., Escobar, R., Colle, S., 2018. Multi-objective optimization of hybrid CSP+PV system using genetic algorithm. Energy 147, 490–503. https://doi.org/10.1016/j.energy.2017.12.116

Variés, 2009. List of solar thermal power stations, section: Under construction. Wikipedia.

Wagner, M.J., Gilman, P., 2011. Technical Manual for the SAM Physical Trough Model. National Renewable Energy Lab.(NREL), Golden, CO (United States), Golden, CO (United States). https://doi.org/10.2172/1016437

Wang, K., Pantaleo, A., Herrando, M., Pesmazoglou, I., Franchetti, B., Markides, C.N., 2019. Thermoeconomic assessment of a spectral splitting hybrid PVT system in dairy farms for

combined heat and power, in: Proceedings of the 32nd International Conference on Efficiency, Cost, Optimization, Simulation and Environmental Impact of Energy Systems (ECOS). pp. 23–28.

Widyolar, B., Jiang, L., Winston, R., 2018. Spectral beam splitting in hybrid PV/T parabolic trough systems for power generation. Appl. Energy 209, 236–250. https://doi.org/10.1016/j.apenergy.2017.10.078

Woodhouse, M., Smith, B., Ramdas, A., Margolis, R., 2019. Crystalline Silicon Photovoltaic Module Manufacturing Costs and Sustainable Pricing: 1H 2018 Benchmark and Cost Reduction Road Map. Golden, CO (United States).

Xu, Q., Ji, Y., Riggs, B., Ollanik, A., Farrar-Foley, N., Ermer, J.H., Romanin, V., Lynn, P., Codd, D., Escarra, M.D., 2016. A transmissive, spectrum-splitting concentrating photovoltaic module for hybrid photovoltaic-solar thermal energy conversion. Sol. Energy 137, 585–593. https://doi.org/10.1016/j.solener.2016.08.057

Appendix A

The coefficients used in the equations for HCE heat losses and piping heat losses are provided in Table A.1 and Table A.2 below:

Table A.1: HCE heat loss coefficients for different operational states.

	Vacuum	Lost Vacuum	Broken Glass
$F_{HeatLoss}$	1	1	1
F_{HL_A0}	4.05	50.8	-9.95
F_{HL_A1}	0.247	0.904	0.465
F_{HL_A2}	-0.00146	0.000579	-0.000854
F_{HL_A3}	5.65e-06	1.13e-05	1.85e-05
F_{HL_A4}	7.62e-08	1.73e-07	6.89e-07
F_{HL_A5}	-1.7	-43.2	24.7
F_{HL_A6}	0.0125	0.524	3.37

Table A.2: Piping heat loss coefficients.

F_{PHL_A1}	0.001693
F_{PHL_A2}	-1.683e-05
F_{PHL_A3}	6.78e-08
$Q_{PHL_DesignT}$	10 W/m^2

The coefficients used in calculating parasitic losses in heat transfer fluid pump and the balance of plant are provided in Table A.3.

Table A.3: Parasitic loss coefficients for heat transfer fluid pump and balance of plant.

	$P_{loss,system\ design}$	F_0	F_1	F_2
$P_{loss,HTFpump}$	1.052e-05 MWe/m^2	-0.036	0.242	0.794
$P_{loss,BoP}$	0.02467 MWe/MWe	0.483	0.517	0.0